



# 1 Estimating global ammonia (NH<sub>3</sub>) emissions based on IASI 2 observations from 2008 to 2018

3  
4 Zhenqi Luo<sup>1, 2</sup>, Yuzhong Zhang<sup>1, 2, \*</sup>, Wei Chen<sup>1, 2</sup>, Martin Van Damme<sup>3, 4</sup>, Pierre-François Coheur<sup>3</sup>,  
5 Lieven Clarisse<sup>3</sup>

6 <sup>1</sup>Key Laboratory of Coastal Environment and Resources of Zhejiang Province, School of Engineering, Westlake University,  
7 Hangzhou, Zhejiang Province, 310024, China

8 <sup>2</sup>Institute of Advanced Technology, Westlake Institute for Advanced Study, Hangzhou, Zhejiang Province, 310024, China

9 <sup>3</sup>Université libre de Bruxelles (ULB), Spectroscopy, Quantum Chemistry and Atmospheric Remote Sensing (SQUARES),  
10 Brussels, Belgium

11 <sup>4</sup>BIRA-IASB - Belgian Institute for Space Aeronomy, Brussels, Belgium

12

13 *Correspondence to:* Y. Zhang (zhangyuzhong@westlake.edu.cn), Z. Luo (zl725@cornell.edu)

14 **Abstract.** Emissions of ammonia (NH<sub>3</sub>) to the atmosphere impact human health, climate, and ecosystems through their  
15 critical contributions to secondary aerosol formation. Estimation of NH<sub>3</sub> emissions is associated with large uncertainties  
16 because of inadequate knowledge about agricultural sources. Here, we use satellite observations from the Infrared  
17 Atmospheric Sounding Interferometer (IASI) and simulations from the GEOS-Chem model to constrain global NH<sub>3</sub>  
18 emissions over the period of 2008-2018. We update the prior NH<sub>3</sub> emission fluxes with the ratio between biases in simulated  
19 NH<sub>3</sub> concentrations and effective NH<sub>3</sub> lifetimes against the loss of the NH<sub>x</sub> family. In contrast to about a factor of two  
20 discrepancies between top-down and bottom-up emissions found in previous studies, our method results in a global land NH<sub>3</sub>  
21 emission of 79 (71-96) Tg a<sup>-1</sup>, ~30 % higher than the bottom-up estimates. Regionally, we find that the bottom-up inventory  
22 underestimates NH<sub>3</sub> emissions over the South America and tropical Africa by 60-70 %, indicating under-representation of  
23 agricultural sources in these regions. We find a good agreement within 10 % between bottom-up and top-down estimates  
24 over the U.S., Europe and eastern China. Our results also show significant increases in NH<sub>3</sub> emissions over India (13 %  
25 decade<sup>-1</sup>), tropical Africa (33 % decade<sup>-1</sup>), and South America (18 % decade<sup>-1</sup>) during our study period, consistent with the  
26 intensifying agricultural activities in these regions in the past decade. We find that inclusion of SO<sub>2</sub> column observed by  
27 satellite is crucial for more accurate inference of NH<sub>3</sub> emission trends over important source regions such as India and China  
28 where SO<sub>2</sub> emissions have changed rapidly in recent years.

## 29 1 Introduction

30 Emissions of ammonia (NH<sub>3</sub>) to the atmosphere has critical implications for human health, climate, and ecosystems. As the  
31 main alkaline gas, NH<sub>3</sub> reacts with acidic products from precursors such as NO<sub>x</sub> and SO<sub>2</sub> to form fine particulate matters,  
32 which is a well-documented risk factor for human health, causing great welfare loss globally (Erisman 2021; Gu et al., 2021).



33 These particulate matters also affect the Earth's radiative balance by directly scattering incoming radiation (Ma et al., 2012)  
34 and indirectly as cloud condensation nuclei (Höpfner et al., 2019). Additionally, both gas-phase ammonia ( $\text{NH}_3$ ) and aerosol-  
35 phase ammonium ( $\text{NH}_4^+$ ) can deposit onto the surface of land and water through dry and wet processes, and therefore are  
36 associated with soil acidification (Zhao et al., 2009), ecosystem eutrophication (Dirnböck et al., 2013), biodiversity loss  
37 (Stevens et al., 2010), and cropland nitrogen uptake (Liu et al., 2013).

38  $\text{NH}_3$  is emitted from a variety of anthropogenic and natural sources, including agriculture, industry, fossil fuel combustion,  
39 biomass burning, natural soils, ocean, and wild animals (Behera et al., 2013). Among these, agricultural activities, mainly  
40 livestock manure management and mineral fertilizer application, are the most important  $\text{NH}_3$  sources, which account for ~70%  
41 of the total  $\text{NH}_3$  emissions globally (Bouwman et al., 1997; Sutton et al., 2013).  $\text{NH}_3$  emissions can be estimated with a  
42 bottom-up approach based on information of emission activities and emission factors (Hoesly et al., 2018; Crippa et al.,  
43 2021). However, bottom-up estimates of  $\text{NH}_3$  emissions are generally thought to be uncertain, relative to other pollutants that  
44 are mainly from fossil fuel combustion sources (e.g.,  $\text{NO}_x$ , CO). One of the challenges is that the intensity of agricultural  
45  $\text{NH}_3$  emissions, emission factors, either from livestock or fertilizer, depend strongly on management and farming practices,  
46 but this information is usually not widely available (Zhang et al., 2017). Furthermore, microbial activities that are  
47 responsible for agricultural  $\text{NH}_3$  emissions are highly variable and has a complex dependence on environmental conditions,  
48 which is often inadequately captured by bottom-up approaches (Behera et al., 2013; Vira et al., 2021). In many cases,  
49 emission factors used in bottom-up modelling are based on local studies that are not representative for the diversity of  
50 conditions and not depending on meteorological parameters.

51 Top-down analyses of atmospheric observations (e.g.,  $\text{NH}_3$  concentrations or  $\text{NH}_4^+$  depositional fluxes) provide an alternative  
52 constraint on  $\text{NH}_3$  emissions. For example, observations of  $\text{NH}_3$  concentrations and  $\text{NH}_4^+$  deposition fluxes from surface  
53 networks can be used to infer regional  $\text{NH}_3$  emission fluxes (e.g., Paulot et al., 2014). However, surface sites are often sparse,  
54 especially in developing continents such as Africa and South America, limiting our capability to constrain  $\text{NH}_3$  emissions  
55 globally. The advent of satellite observations makes it possible to investigate long-term spatially resolved  $\text{NH}_3$  emissions  
56 from national, continental, to global scales. Van Damme et al. (2018) reported large  $\text{NH}_3$  point sources across the globe that  
57 are detected by the Infrared Atmospheric Sounding Interferometer (IASI) instrument but missing in the bottom-up  
58 inventories. Studies have also applied satellite data (e.g., IASI and Cross-track Infrared Sounder (CrIS)) to study  $\text{NH}_3$   
59 emissions from important source regions, including the U.S. (Cao et al., 2020; Chen et al., 2021b), China (Zhang et al.,  
60 2018), and Europe (Marais et al., 2021; van der Graaf et al., 2021). These regional studies show 20 % to 50 % differences  
61 between top-down and bottom-up estimates of  $\text{NH}_3$  emissions.

62 Compared to regional analyses, long-term global analyses of  $\text{NH}_3$  emissions based on satellite observations are relatively  
63 scarce (e.g., Evangeliou et al., 2021). This is partly because of the computational challenges arising from a full-fledged  
64 inversion for a long period of time and over large spatial extents. In a recent study, Evangeliou et al. (2021) proposed a fast  
65 top-down method, in which  $\text{NH}_3$  emissions are computed as the ratio between  $\text{NH}_3$  column observations and  $\text{NH}_3$  lifetime.  
66 This method relies on  $\text{NH}_3$  lifetime diagnosed from a chemical transport model (CTM) and assumes a local mass balance.



67 Their analysis found a global  $\text{NH}_3$  emission of around 180  $\text{Tg a}^{-1}$ , which is roughly triple the widely used bottom-up  
68 estimates (e.g., 62  $\text{Tg a}^{-1}$  by the Community Emission Data System, CEDS). This large upward adjustment, if true, would  
69 have huge implications for global reactive nitrogen cycles and indicate that our current understanding of global  $\text{NH}_3$   
70 emissions is seriously flawed.

71 In this paper, we examine if the large discrepancy between the bottom-up and top-down estimates is due to the methodology.  
72 We refine the fast top-down approach by improving  $\text{NH}_3$  lifetime diagnosis and partially accounting for the transport  
73 contributions. We develop a series of data filtering procedures to exclude results that are not sufficiently constrained by  
74 observations or affected by large deviations from the assumption of the fast top-down method. We apply the updated method  
75 to IASI observations to derive the global distribution of  $\text{NH}_3$  emissions fluxes from 2008 to 2018, and examine the impact of  
76 the improved method on global  $\text{NH}_3$  emission inferences. Finally, we evaluate the consistency of varied top-down and  
77 bottom-up estimates against IASI observations with full-chemistry simulations.

## 78 **2 Methods**

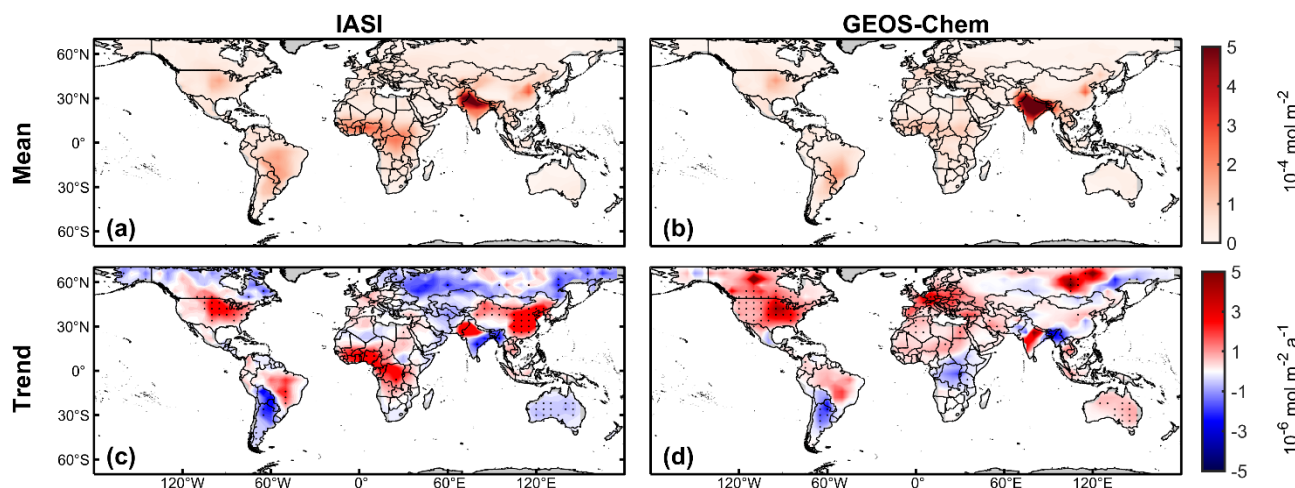
### 79 **2.1 IASI observations**

80 We use 2008–2018  $\text{NH}_3$  total column retrievals (ANNI- $\text{NH}_3$ -v3R) from the IASI on board Metop-A. The IASI instrument  
81 measures the infrared radiation ( $645\text{--}2760\text{ cm}^{-1}$ ) from Earth's surface and the atmosphere with a circular 12 km footprint at  
82 nadir (Clerbaux et al., 2009; Van Damme et al., 2017). The retrieval algorithm calculates the hyperspectral range index from  
83 IASI spectra measurements (Van Damme et al., 2014) and converts it to the  $\text{NH}_3$  total column density via an artificial neural  
84 network (Whitburn et al., 2016; Franco et al., 2018). The retrieval uses consistent meteorological data from the ERA5  
85 reanalysis, so it is suitable for the analyses of inter-annual variability and long-term trends (Hersbach et al., 2020). The  
86 ANNI- $\text{NH}_3$ -v3R product, has been validated against in situ measurements and is shown to have a good regional correlation  
87 (Guo et al., 2021; Van Damme et al., 2021). The dataset has been used in previous studies to estimate  $\text{NH}_3$  emissions  
88 globally (e.g., Evangelidou et al., 2021) and regionally (e.g., Chen et al., 2021b; Marais et al., 2021).

89 Here we only use morning  $\text{NH}_3$  data (around 9:30 local solar time) though IASI provides global coverage twice daily,  
90 because of the better precision of morning observations resulting from favorable thermal contrast conditions (Clarisse et al.  
91 2010). We filter out data with a cloud fraction greater than 10 % (Van Damme et al., 2018) and a skin temperature below  
92 263 K (Van Damme et al., 2014). The skin temperature dataset is from ERA5 (Hersbach et al., 2020). To compare with  
93 simulated  $\text{NH}_3$  columns (see Sect. 2.2), we regrid and average monthly IASI  $\text{NH}_3$  observations on the GEOS-Chem  $4^\circ \times 5^\circ$   
94 grid (Fig. 1a). To reduce uncertainty from sparse sampling, we further exclude grid cells with the number of successful  
95 retrievals less than 800 in a month. We also test the choices of the threshold for 400 and 1200 per month in the sensitivity  
96 calculations (Table S1, line 5–6). This criterion affects mainly high latitudes during wintertime, where snow surfaces make it  
97 unfavourable for infrared measurements (Fig. S1).



98



99

100 **Figure 1.** Spatial distribution of (a, c) IASI and (b, d) GEOS-Chem NH<sub>3</sub> column concentrations. (a, b) Mean and (c, d) linear trends within  
101 the 70°N–70°S during 2008–2018. Dots in (c) and (d) indicate that linear trends are significant at the 95 % confidence levels. Linear trends  
102 are computed from the time series of annual averages.

## 103 2.2 GEOS-Chem simulations

104 We use the GEOS-Chem CTM v12.9.3 (10.5281/zenodo.3974569) to simulate global NH<sub>3</sub> concentrations. The GEOS-Chem  
105 model, driven by the MERRA-2 reanalyzed meteorology (Gelaro et al., 2017), simulates the tropospheric ozone–NO<sub>x</sub>–  
106 VOCs–aerosol chemistry at 4° × 5° resolution with 47 vertical layers (30 layers in the troposphere) (Bey et al., 2001; Park et  
107 al., 2004). The thermodynamic equilibrium between gas phase NH<sub>3</sub> and aerosol phase NH<sub>4</sub><sup>+</sup> is explicitly simulated by the  
108 ISORROPIA-II module in GEOS-Chem (Fountoukis & Nenes, 2007). The model also simulates the wet and dry deposition  
109 of NH<sub>3</sub> and NH<sub>4</sub><sup>+</sup>, the terminal sinks of atmospheric NH<sub>x</sub> (≡ NH<sub>3</sub> + NH<sub>4</sub><sup>+</sup>). Dry deposition is represented with a resistances-  
110 in-series scheme (Wesely, 2007) and wet deposition includes scavenging in convective updrafts and in- and below-cloud  
111 scavenging from large-scale precipitation (Wang et al., 2011; Amos et al., 2012). Anthropogenic emissions of simulated  
112 chemicals including those of NH<sub>3</sub> are taken from a global emission inventory CEDS (Hoesly et al., 2018), overridden by  
113 regional inventories in Canada (Air Pollutant Emission Inventory, APEI), the United States (2011 National Emissions  
114 Inventory, NEI-2011), Asia (MIX-Asia v1.1) (Li et al., 2017), and Africa (DICE-Africa) (Eloise Marais and Christine  
115 Wiedinmyer, 2016). Such compiled anthropogenic emissions only include incomplete information on inter-annual trends  
116 because inventories are not all available throughout the whole period. Anthropogenic emissions are essentially invariant after  
117 2013 in our setup (Fig. S2). The general lack of trends in SO<sub>2</sub> emissions in the simulation, if not accounted for, may cause  
118 biases in inferred trends over regions such as India and China where SO<sub>2</sub> emissions have changed rapidly (Sun et al., 2018;  
119 Qu et al., 2019; Chen et al., 2021a). Fire emissions are from Global Fire Emissions Database (GFED4) (van der Werf et al.,  
120 2017), and biogenic VOC emissions are from the Model of Emissions of Gases and Aerosols from Nature (MEGAN)  
121 (Guenther et al., 2012). Temporal (seasonal and inter-annual) variations in fire and biogenic emissions are resolved by the  
122 inventories. Hereafter, we refer to NH<sub>3</sub> emissions from this set of inventories as BUE1. For comparison, we also use another



123 set of bottom-up inventories which consist of EDGARv5.0 for anthropogenic emissions  
124 (<https://data.jrc.ec.europa.eu/collection/edgar>, last access: 8 March 2022, [Crippa et al., 2020](#)), GFAS for fire emissions  
125 (CAMS, <https://apps.ecmwf.int/datasets/data/cams-gfas/>, last access: 8 March 2022) (minor natural emissions are the same  
126 as BUE1), which we denote as BUE2.

127 The GEOS-Chem simulation is conducted from 2008 to 2018 with an additional 1-month spin-up starting from December  
128 2007. We sample the simulated  $\text{NH}_3$  and  $\text{NH}_4^+$  concentration fields between 9:00 to 10:00 local solar time, approximately the  
129 IASI morning overpass time. To compare with the IASI  $\text{NH}_3$  columns, we integrate the vertical profiles of simulated  $\text{NH}_3$   
130 concentrations by layer thickness. The ANNI- $\text{NH}_3$ -v3R retrieval algorithm does not provide information on the vertical  
131 sensitivity of the IASI measurements (i.e., averaging kernels) ([Van Damme et al., 2017](#)). In addition, we also archive  
132 depositional and transport rates for  $\text{NH}_3$  and  $\text{NH}_4^+$ , which are used in emission fluxes estimation.

### 133 2.3 $\text{NH}_3$ emission fluxes estimation

134 We compute the top-down  $\text{NH}_3$  emission fluxes (TDE) ( $\hat{E}_{\text{NH}_3}$ , in molecules  $\text{m}^{-2} \text{s}^{-1}$ ) in land grid cells for individual months  
135 from 2008 to 2018. We update the prior model emission fluxes ( $E_{\text{NH}_3,\text{mod}}$ , in molecules  $\text{m}^{-2} \text{s}^{-1}$ ) with a correction term  
136 positively proportional to the difference of observed ( $C_{\text{NH}_3,\text{obs}}$ , in molecules  $\text{m}^{-2}$ ) and simulated ( $C_{\text{NH}_3,\text{mod}}$ , in molecules  $\text{m}^{-2}$ )  
137  $\text{NH}_3$  total column densities and inversely proportional to the lifetime of  $\text{NH}_3$  ( $\tau_{\text{NH}_3,\text{mod}}$ , in s):

$$138 \quad \hat{E}_{\text{NH}_3} = E_{\text{NH}_3,\text{mod}} + \frac{C_{\text{NH}_3,\text{obs}} - C_{\text{NH}_3,\text{mod}}}{\tau_{\text{NH}_3,\text{mod}}}, \quad (1)$$

139 where  $\tau_{\text{NH}_3,\text{mod}}$  is computed as the ratio of the simulated  $\text{NH}_3$  column and the sum of simulated loss rate of the  $\text{NH}_x$  family  
140 ( $\text{NH}_x \equiv \text{NH}_3 + \text{NH}_4^+$ ) through the dry and wet depositions of  $\text{NH}_3$  ( $D_{\text{NH}_3,\text{mod}}$ , in molecules  $\text{m}^{-2} \text{s}^{-1}$ ) and  $\text{NH}_4^+$  ( $D_{\text{NH}_4^+,\text{mod}}$ , in  
141 molecules  $\text{m}^{-2} \text{s}^{-1}$ ):

$$142 \quad \tau_{\text{NH}_3,\text{mod}} = \frac{C_{\text{NH}_3,\text{mod}}}{D_{\text{NH}_3,\text{mod}} + D_{\text{NH}_4^+,\text{mod}}}. \quad (2)$$

143 Here we consider the loss of the  $\text{NH}_x$  family rather than that of  $\text{NH}_3$ , because the fast thermodynamic equilibrium between  
144 gas-phase  $\text{NH}_3$  and aerosol/aqueous-phase  $\text{NH}_4^+$  implies that the conversion from  $\text{NH}_3$  to  $\text{NH}_4^+$  is not a terminal loss for  $\text{NH}_3$   
145 from the atmosphere. The  $\text{NH}_3$  lifetime may be underestimated over source regions and overestimated over remote regions,  
146 if  $\text{NH}_3$  to  $\text{NH}_4^+$  conversions are treated as a terminal loss as in [Evangelou et al. \(2021\)](#) rather than a partition within a  
147 chemical family as in [Eq. \(2\)](#).

148 In addition, our method linearizes the column-emission relationship at prior emissions as opposed to zero emissions in the  
149 previous method (e.g., [Evangelou et al., 2021](#)). Here, the baseline  $\text{NH}_3$  column ( $C_{\text{NH}_3,\text{mod}}$ ) simulated by the GEOS-Chem  
150 model explicitly accounts for the non-local contribution of transport, while the correction to prior emissions is done only  
151 locally, that is, the difference between  $C_{\text{NH}_3,\text{obs}}$  and  $C_{\text{NH}_3,\text{mod}}$  is attributed only to errors in local emissions without  
152 accounting for the sensitivity to emissions from other grid cells. This hybrid approach can partially include the non-local



153 contribution from transport but still keeps the computation tractable for a long-term study such as this study, striking a trade-  
154 off between the computational efficiency of a local method (e.g., [Van Damme et al., 2018](#); [Evangelidou et al., 2021](#)) and the  
155 accuracy of a full-fledged inversion (e.g., [Cao et al., 2020](#); [Chen et al., 2021b](#)). The errors arising from local correction of  
156 NH<sub>3</sub> emissions are expected to be small in most cases, because the NH<sub>3</sub> lifetime is short relative to a typical transport time  
157 across a 4° × 5° grid cell on which emissions are estimated. To identify cases when this error is not negligible, we apply a  
158 monthly NH<sub>x</sub> budget analysis based on the GEOS-Chem simulation and exclude grid cells from our analysis where transport  
159 dominates over local prior emissions or depositions in the monthly NH<sub>3</sub> budget (Transport/Emission>1 or  
160 Transport/Deposition>1). We also test the impact of alternative thresholds (0.2 and 5) on NH<sub>3</sub> emission estimations (**Table**  
161 **S1**, Line 7-8). This procedure mostly affects remote regions where emissions are small, notably northern high latitudes (**Fig.**  
162 **S3**).

163 Because rapid changes in SO<sub>2</sub> emissions in eastern China and India, particularly after 2012, are not captured by our prior  
164 simulation (**Fig. S2**), the estimation of NH<sub>3</sub> emission trends using **Eq. (1)** may be biased over these regions. To address this  
165 issue, we further modify **Eq. (1)** to include observed trends in SO<sub>2</sub> column concentrations:

$$166 \quad \hat{E}_{\text{NH}_3, \text{SO}_2\text{-correct}} = E_{\text{NH}_3, \text{mod}} + \frac{C_{\text{NH}_3, \text{obs}} - C_{\text{NH}_3, \text{mod}} + 2\omega C_{\text{SO}_4^{2-}, \text{mod}}}{\tau_{\text{NH}_3, \text{mod}}}, \quad (3)$$

167 where  $\omega$  (%) is the fractional changes of average SO<sub>2</sub> columns relative to the baseline year (i.e., 2012) over China or India  
168 and  $C_{\text{SO}_4^{2-}, \text{mod}}$  (molecules m<sup>-2</sup> s<sup>-1</sup>) is the simulated column densities of aerosol sulfate. Here, we specify a linear trend of -5 %  
169 yr<sup>-1</sup> for eastern China and 5 % yr<sup>-1</sup> for India between 2012 and 2018, based on values derived from the ozone monitoring  
170 instrument (OMI) and Ozone Mapping and Profiler Suite (OMPS) observations ([Wang and Wang, 2020](#); [Liu et al., 2018](#)).  
171 The factor 2 accounts for the fact that two molecules of NH<sub>3</sub> are required to neutralize one molecule of H<sub>2</sub>SO<sub>4</sub>. **Eq. (3)** only  
172 applies when NH<sub>3</sub> is in excess, a condition usually met in eastern China and India but not necessarily elsewhere ([Lachatre et](#)  
173 [al., 2019](#); [Acharja et al., 2022](#)). Therefore, we only apply **Eq. (3)** to eastern China and India to understand the impact of  
174 changing SO<sub>2</sub> emissions on the inference of NH<sub>3</sub> emission trends. To use SO<sub>2</sub> observations systematically in NH<sub>3</sub> emission  
175 estimations requires further investigations.

## 176 2.4 Uncertainty and sensitivity analysis

177 We perform a series of perturbation and sensitivity experiments to assess the uncertainty of our estimates (**Table S1**). We  
178 perturb  $C_{\text{NH}_3, \text{mod}}$  and  $\tau_{\text{NH}_3, \text{mod}}$  in **Eq. (1)**. The perturbations to  $\tau_{\text{NH}_3, \text{mod}}$  are set to be 50 % and 200 % (**Table S1**, Line 1-2).  
179 The perturbation to  $C_{\text{NH}_3, \text{mod}}$  is set to be the standard deviation of monthly mean column concentrations ( $\sigma_{\text{C, obs}}$ ) (**Table S1**,  
180 Line 3-4), which is related to the number of IASI measurements ( $n$ ) and their measurement errors:

$$181 \quad \sigma_{\text{C, obs}} = \sqrt{\frac{\sum_{i=1}^{i=n} (\sigma_i \times \Omega_i)^2}{n - 1}}, \quad (4)$$



182 where  $\Omega_i$  (in mol m<sup>-2</sup>) is the  $i^{\text{th}}$  NH<sub>3</sub> column measurement out of a total number of  $n$  observations in a grid cell during a  
183 month and  $\sigma_i$  is the relative error reported in the IASI product. We then use  $\Omega \pm \sigma_{C,obs}$  to evaluate the effect of measurement  
184 errors in emission estimates (**Table S1**, Line 3-4). We also conduct sensitivity tests by using alternative parameters in data  
185 filtering (**Table S1**, Line 5-8).

186 In addition, we perform GEOS-Chem full chemistry simulations in selected years (2008, 2013, 2018) to examine the  
187 consistency of NH<sub>3</sub> emission estimates with the IASI observations. We use our top-down estimate (TDE) and prior  
188 emissions (BUE1) to drive the full chemistry simulation. We compute the fractional biases (FBs) of these simulations against  
189 the IASI observations to evaluate the systematic biases in the resulting NH<sub>3</sub> column density fields:

$$190 \quad FB = 2 \times \frac{\sum_{i=1}^{i=N} (C_{mod,i} - C_{obs,i})}{\sum_{i=1}^{i=N} (C_{mod,i} + C_{obs,i})}. \quad (5)$$

## 191 **3 Results and discussion**

### 192 **3.1 Observed and simulated NH<sub>3</sub> concentrations**

193 **Fig. 1a and 1b** plot observed and simulated NH<sub>3</sub> total column concentrations averaged over 2008-2018. The GEOS-Chem  
194 simulation generally reproduces the global distribution of NH<sub>3</sub> concentrations observed by the IASI instrument. Good  
195 agreements (i.e., difference < 10 %) are found in the U.S., Europe, and southern South America. Meanwhile, the GEOS-  
196 Chem model underestimates NH<sub>3</sub> concentrations in eastern China, northern South America, and tropical Africa by 20-120 %,   
197 and overestimates in southern India by around 50 %, indicating biases in NH<sub>3</sub> emissions over these regions.

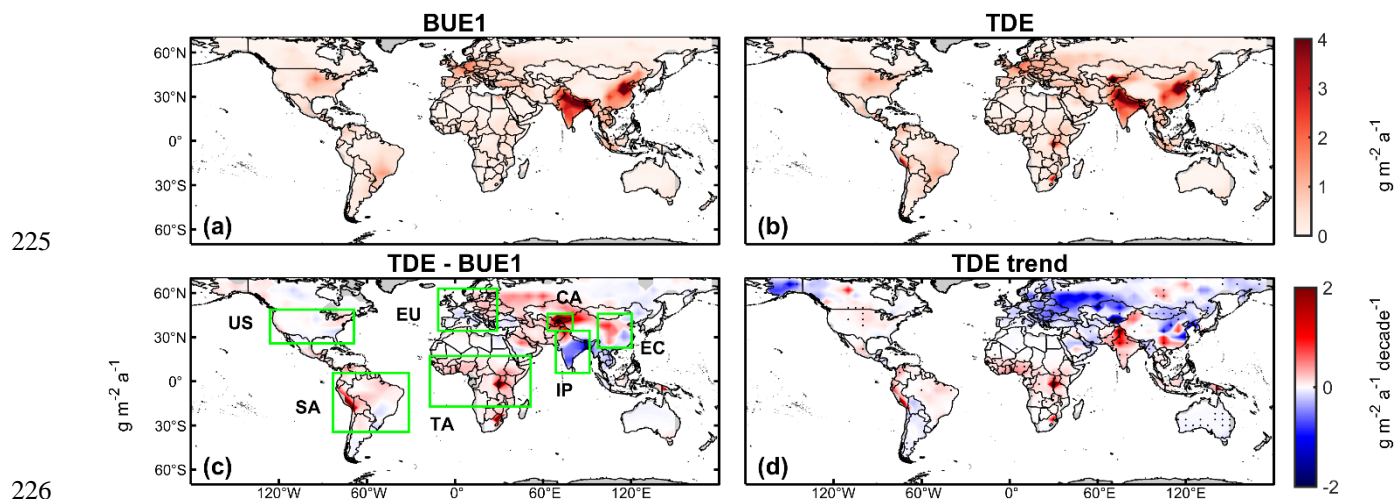
198 **Fig. 1c and 1d** show 2008-2018 linear trends in NH<sub>3</sub> column concentrations derived from the IASI observations and the  
199 GEOS-Chem simulations. The linear trends are computed based on the time series of annual averages. The IASI trends  
200 shown in Fig. 1c are in general consistent with a recent analysis by Van Damme et al. (2021). IASI observes a positive NH<sub>3</sub>  
201 concentration trend of 2.9 % a<sup>-1</sup> over the U.S., and this trend is well captured by GEOS-Chem. Similarly, the observation and  
202 the simulation agree on a dipole pattern in South America (i.e., positive trend in Brazil and negative trend in Argentina).  
203 Because anthropogenic emissions over this region are set to be invariant in our simulation (**Fig. S2**), this agreement suggests  
204 that these trends are due to meteorological conditions and/or fire emissions, rather than changes in anthropogenic emissions.  
205 The satellite also observes significant positive trends in NH<sub>3</sub> concentrations over China (5.2 % a<sup>-1</sup>) and tropical Africa (2.0 %  
206 a<sup>-1</sup>), but these trends are not reproduced in the simulation (0.3 % a<sup>-1</sup> for China and 0.2 % a<sup>-1</sup> for tropical Africa). These  
207 simulation-observation differences can not only reflect discrepancies in the trends of anthropogenic NH<sub>3</sub> emissions, but also  
208 be attributed to uncaptured changes in SO<sub>2</sub> and/or NO<sub>x</sub> emissions in these regions. We also find that a positive NH<sub>3</sub>  
209 concentration trend over Europe appears in the simulation (3.0 % a<sup>-1</sup>) but is much weaker (1.0 % a<sup>-1</sup>) in the observation,  
210 suggesting decreasing emissions after 2013. Both the satellite and model do not find significant trends in NH<sub>3</sub> concentrations  
211 over India (absolute value less than 1 % yr<sup>-1</sup>). Strong GEOS-Chem trends in eastern Canada and Siberia result from large



212 wildfires that occurred in the latter part of the study period. IASI trends in northern boreal regions are less robust because of  
213 noisy and sparse measurements over high latitudes (**Fig. S1**).

### 214 3.2 NH<sub>3</sub> emissions inferred from IASI observations

215 **Fig. 2** shows the spatial distributions of NH<sub>3</sub> emission fluxes and their 2008–2018 linear trends inferred from IASI  
216 observations using the method described in **Sect. 2.3**. **Fig. 3** plots annual time series aggregated for seven selected regions.  
217 The top-down estimate (TDE) suggests upward adjustments in NH<sub>3</sub> emissions over South America (SA) by 62 %, tropical  
218 Africa (TA) by 69 %, and Central Asia (CA) by 327 %, relative to the prior inventory (BUE1), but downward adjustments in  
219 NH<sub>3</sub> emissions by 14 % in India Peninsula (IP) and by 33 % in Canada. After accounting for the contributions from natural  
220 emissions including fires, we find that most of these biases in NH<sub>3</sub> emissions can be attributed to anthropogenic sources,  
221 except for Canada where the underestimation appears to relate to fire emissions. This result reflects a general inadequate  
222 representation of agricultural and industrial emissions from developing continents in current global emission inventories.  
223 The TDE finds good agreements with the BUE1 (difference within 10 %) over the U.S., Europe (EU), eastern China (EC)  
224 and Australia.

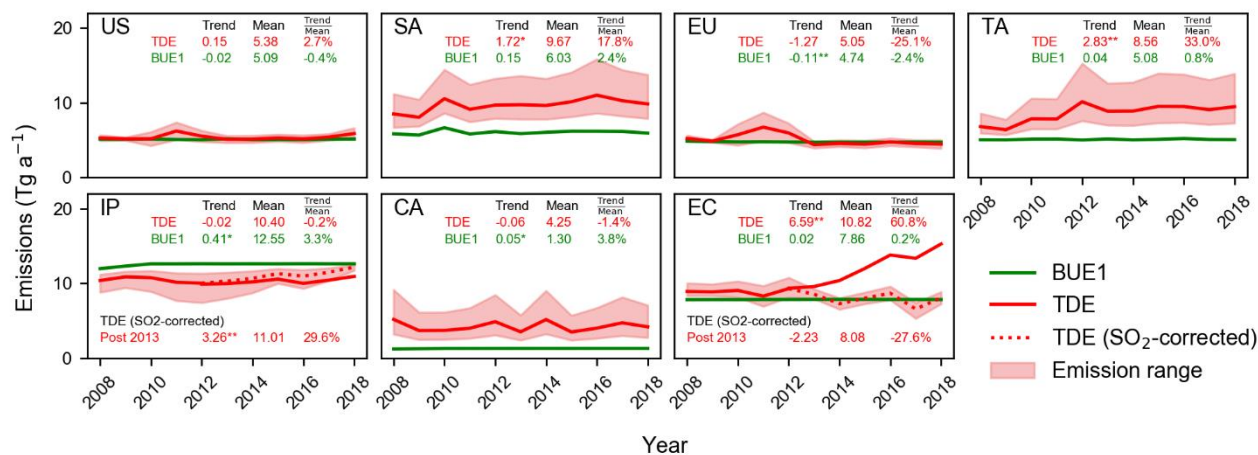


227 **Figure 2.** Spatial distribution of NH<sub>3</sub> emission fluxes during 2008–2018. (a) Bottom-up emissions (BUE1), (b) top-down emissions (TDE)  
228 inferred from IASI observations, (c) difference between TDE and BUE1 estimates and (d) emission trends derived from TDE estimates.  
229 Green boxes denote seven regions analysed in Sect. 3.2. Top-down emission fluxes are computed with Eq. (1) except for IP and EC where  
230 Eq. (3) is applied. Linear trends are computed from the time series of annual averages. Dots in (d) represent significant linear trends at the  
231 95 % confidence level.

232 In addition to the adjustments in average emissions, the TDE also detects changes in NH<sub>3</sub> emissions during the period of  
233 2008–2018, as expressed in linear trends computed from annual time series. We find significant positive emission trends in  
234 SA (1.7 Tg a<sup>-1</sup> decade<sup>-1</sup> or 18 % decade<sup>-1</sup>) and TA (2.8 Tg a<sup>-1</sup> decade<sup>-1</sup> or 33 % decade<sup>-1</sup>) (**Fig. 3**). These increases are  
235 concurrent with intensifying agricultural activities in these regions (Warner et al., 2017; E. Hickman et al., 2020), except for  
236 a 2010 peak over SA, which coincides with fires in savanna and evergreen forests there (Chen et al., 2013). Comparison with

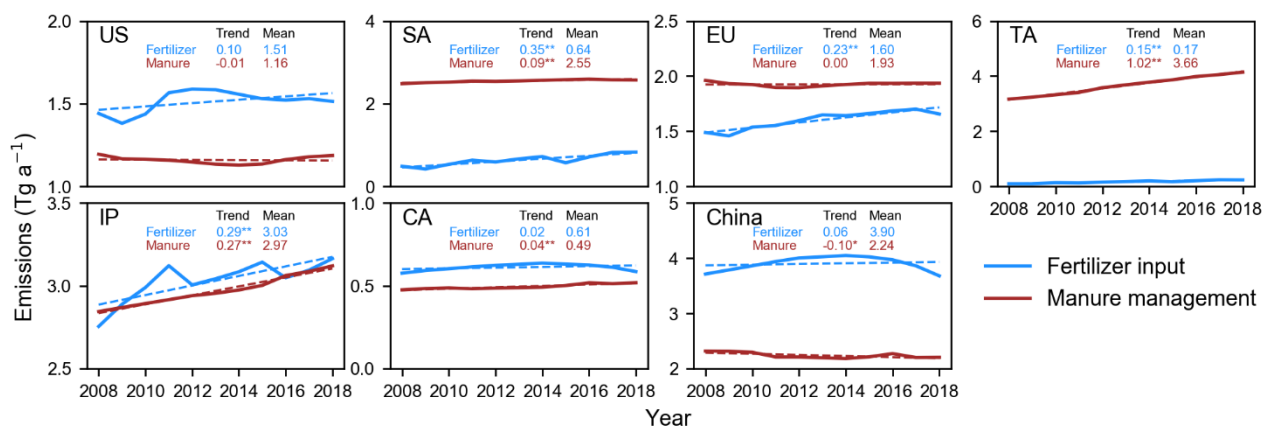


237 data from the Food and Agriculture Organization of the United Nations (FAO) (<http://www.fao.org/faostat>, last access: 7  
 238 July 2021) suggests that the increase in SA is driven primarily by growing application of synthetic fertilizer (55 % decade<sup>-1</sup>),  
 239 whereas the increase in TA is consistent with increasing manure amount (28 % decade<sup>-1</sup>) from a growing livestock  
 240 population (E. Hickman et al., 2021) (Fig. 4).



241

242 **Figure 3.** Annual NH<sub>3</sub> emissions for seven selected regions during 2008-2018. Shadings represent the range derived from uncertainty  
 243 analyses (see Sect. 2.4). Average annual emissions (Tg a<sup>-1</sup>), absolute linear trends (Tg a<sup>-1</sup> decade<sup>-1</sup>) and relative trends (% decade<sup>-1</sup>) for  
 244 2008-2018 are inset. The asterisk symbols “\*” and “\*\*” represent that linear trends are significant at the 95 % and 99 % confidence level,  
 245 respectively. Red dashed lines represent top-down NH<sub>3</sub> emission estimates over IP and EC during 2013-2018, based on Eq. (3) that  
 246 accounts for observed trends of SO<sub>2</sub> (denoted as “SO<sub>2</sub>-corrected”). Statistics for this estimate are also inset.



247

248 **Figure 4.** Synthetic fertilizer and manure management based on FAO reports (<http://www.fao.org/faostat>) during 2008-2018. To roughly  
 249 compare the contribution from the two sectors, we convert FAO reported statistics to NH<sub>3</sub> emissions (Tg a<sup>-1</sup>) by applying fixed emission  
 250 factors of 13 % for manure N contents (Ma et al., 2020) and 17 % for synthetic fertilizer N contents (Riddick et al., 2016). Values of  
 251 means (Tg a<sup>-1</sup>) and linear trends (Tg a<sup>-1</sup> decade<sup>-1</sup>) are inset. Scales differ between panels.

252 Our results infer large but variable trends over northern high latitudes (e.g., negative trends in Alaska, central Russia, and  
 253 eastern Europe, but positive trends in Canada) (Fig. 2d). Because of large uncertainties associated with high-latitude



254 observations and emission optimization, these trends are less robust but can be partly attributed to variations in fire activities.  
255 Decreases in Russia and eastern Europe are related to wildfire of boreal forests in early part of the study period (2008-2011)  
256 ([Keyword et al., 2012](#); [Warner et al., 2017](#)), while emission increases in Canada is due to wildfire in the late part of the  
257 period (2015) ([Pavlovic et al., 2016](#)). We also infer negative trends ( $-43\% \text{ decade}^{-1}$ ) in Australia, which are statistically  
258 significant, but the absolute magnitude of these trends is small ( $-0.03 \text{ g m}^{-2} \text{ a}^{-1} \text{ decade}^{-1}$  in **Fig. 2d**). The TDE estimation does  
259 not find significant trends in  $\text{NH}_3$  total emissions over the US and Central Asia.

### 260 3.3 Impact of changing $\text{SO}_2$ emissions on $\text{NH}_3$ emission trends over eastern China and India

261 Based on only  $\text{NH}_3$  column measurements (**Eq. (1)**), we also find a decadal increase of  $61\% \text{ decade}^{-1}$  ( $6.6 \text{ Tg a}^{-1} \text{ decade}^{-1}$ ) in  
262  $\text{NH}_3$  emissions over eastern China (**Fig. 3**). This increase is especially large after 2013 and is driven mainly by increases of  
263 IASI  $\text{NH}_3$  column concentration in eastern China (**Fig. 1c**). This large post-2013 increase is inconsistent with flat or even  
264 declining fertilizer input and manure amount (**Fig. 4**). On the other hand, we find no appreciable emission trend in IP (**Fig. 3**),  
265 which appears to agree with relatively stable IASI  $\text{NH}_3$  concentrations over the period (**Fig. 1c**) but is not supported by  
266 increases in fertilizer applications and manure amount shown in the FAO report (**Fig. 4**).

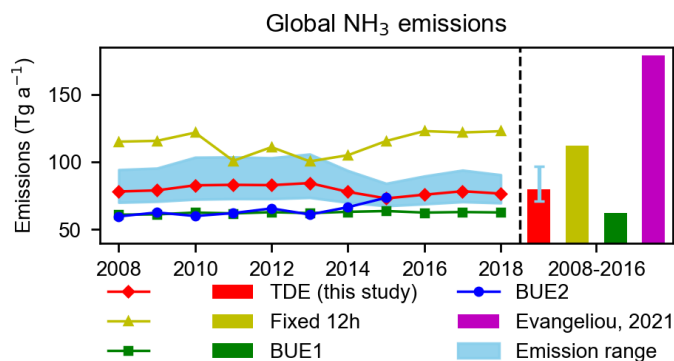
267 An assumption underlying **Eq. (1)** is that the model simulation captures the partition between gas-phase  $\text{NH}_3$  and aerosol-  
268 phase  $\text{NH}_4^+$ . In addition to alkaline  $\text{NH}_3$ , the partition is also determined by the abundance of acids (e.g.,  $\text{H}_2\text{SO}_4$  and  $\text{HNO}_3$ ).  
269 Inaccurate emissions of their precursors (e.g.,  $\text{SO}_2$  and  $\text{NO}_2$ ) in the model simulation, in particular over regions with  
270 excessive  $\text{NH}_3$ , can lead to biases in simulating the  $\text{NH}_3\text{-NH}_4^+$  partition. It is well known that  $\text{SO}_2$  emissions in China have  
271 decreased rapidly after 2013 because of stringent air pollution control measures ([Sun et al., 2018](#); [Zhai et al., 2021](#)), while  
272  $\text{SO}_2$  emissions from India have been increasing ([Qu et al., 2019](#)). But these regional trends are not captured in our prior  
273 simulation due to a lack of emission data (**Fig. S2**).

274 We find that the discrepancies between top-down (**Eq. 1**) and bottom-up estimates of emission trends over EC and IP can be  
275 largely reconciled by including observed  $\text{SO}_2$  column concentrations in the top-down calculation (**Eq. (3)**). By accounting  
276 for OMI and OMPS observed  $\text{SO}_2$  trends ([Wang and Wang, 2020](#)), we derive an overall decreasing  $\text{NH}_3$  emissions in EC  
277 between 2013 and 2018 ( $-2.2 \text{ Tg a}^{-1} \text{ decade}^{-1}$ ,  $-28\% \text{ decade}^{-1}$ ). This result suggests that observed increases in  $\text{NH}_3$  columns  
278 over China are largely explained by decreases in  $\text{SO}_2$  emissions (**Fig. 1** and **Fig. 3**), consistent with previous studies ([Fu et al., 2017](#);  
279 [Liu et al., 2018](#); [Lachatre et al., 2019](#); [Chen et al., 2021a](#)). Bottom-up inventories (e.g., MEIC v1.3, EDGAR v5.0)  
280 also report stable or declining  $\text{NH}_3$  emissions from China during the period (Li et al., 2017; Crippa et al., 2020). Meanwhile,  
281 the revised method (**Eq. (3)**) finds a positive post-2013 trend ( $3.3 \text{ Tg a}^{-1} \text{ decade}^{-1}$ ,  $30\% \text{ yr}^{-1}$ ) in  $\text{NH}_3$  emissions over India.  
282 Compared with our original estimate using **Eq. (1)**,  $\text{NH}_3$  emission trends derived with **Eq. (3)** (i.e., decrease in China and  
283 increase in India after 2013) is more consistent with the bottom-up information of fertilizer input and manure management  
284 (**Fig. 4**). This result demonstrates the potential of assimilating both  $\text{NH}_3$  and  $\text{SO}_2$  satellite observations in constraining  $\text{NH}_3$   
285 emissions, which should be further explored in the future.



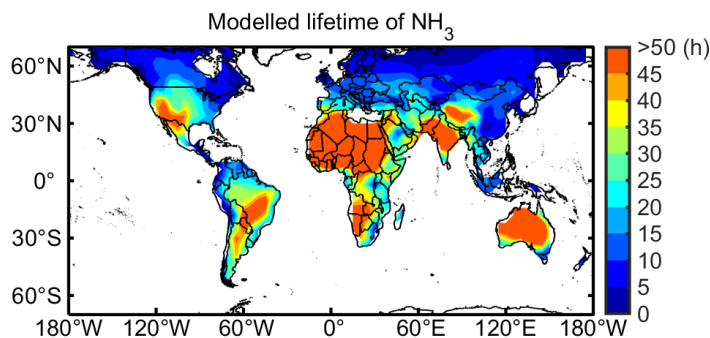
### 286 3.4 Sensitivity of global emission inference to NH<sub>3</sub> lifetime diagnosis

287 Integrating over land areas globally, our IASI-based TDE estimates of NH<sub>3</sub> emissions is 79 (71-96) Tg a<sup>-1</sup> (range of  
288 estimates from uncertainty analysis, see **Table S1**) (**Fig. 5**). This result is about 20-40 % higher than bottom-up inventories  
289 (BUE1, 62 Tg a<sup>-1</sup> and BUE2, 56 Tg a<sup>-1</sup>). In contrast, a previous study by Evangeliou et al. (2021) also based on the IASI data  
290 estimated a much higher global NH<sub>3</sub> emission of 180 Tg a<sup>-1</sup> (**Fig. 5**). One cause of the difference between the two IASI-  
291 based estimates is in diagnosis of NH<sub>3</sub> lifetime from CTM. Evangeliou et al. (2021) treats conversion from NH<sub>3</sub> to NH<sub>4</sub><sup>+</sup> as a  
292 terminal loss and diagnoses NH<sub>3</sub> lifetime averaged 11.6 ± 0.6 h globally from a CTM, which is close to a constant NH<sub>3</sub>  
293 lifetime (12 h) assumed in Van Damme et al. (2018). In this study, we account for the fact that fast thermodynamic  
294 equilibrium can establish between NH<sub>3</sub> and NH<sub>4</sub><sup>+</sup> so that NH<sub>3</sub> can only be terminally lost through the deposition of the NH<sub>x</sub>  
295 family (**Eq. (2)**), which yields a global averaged NH<sub>3</sub> lifetime of 21.2 ± 3.8 h (**Fig. 6**). This longer NH<sub>3</sub> lifetime implies a  
296 higher sensitivity of NH<sub>3</sub> column density to NH<sub>3</sub> emissions, leading to a lower estimate for global NH<sub>3</sub> emissions. In addition,  
297 instead of locally scaling observed NH<sub>3</sub> column by lifetime (Van Damme et al., 2018; Evangeliou et al, 2021; Marais et al.,  
298 2021), our method (**Eq. (1)**) partially accounts for the non-local contribution from transport by including prior NH<sub>3</sub> columns  
299 from a full 3-D simulation and using their difference from observed NH<sub>3</sub> columns to correct prior emissions, which prevents  
300 derivation of large NH<sub>3</sub> emissions in remote regions where observed NH<sub>3</sub> concentrations are driven mainly by transport. Our  
301 data filtering strategy (**Sect 2.1 and 2.2**) is also crucial to avoid spurious top-down results when satellite coverage is poor  
302 and the local mass balance assumption does not hold.



303

304 **Figure 5.** Comparison of our top-down NH<sub>3</sub> emission estimates (TDE) with other top-down (Fixed 12h and Evangeliou et al. (2021)) and  
305 bottom-up (BUE1 and BUE2) results during 2008-2018. The red line and red bar represent central estimates of the TDE, and the blue  
306 shaded area and the blue error bar indicate the uncertainty evaluated by our study (**Sect. 2.4**).

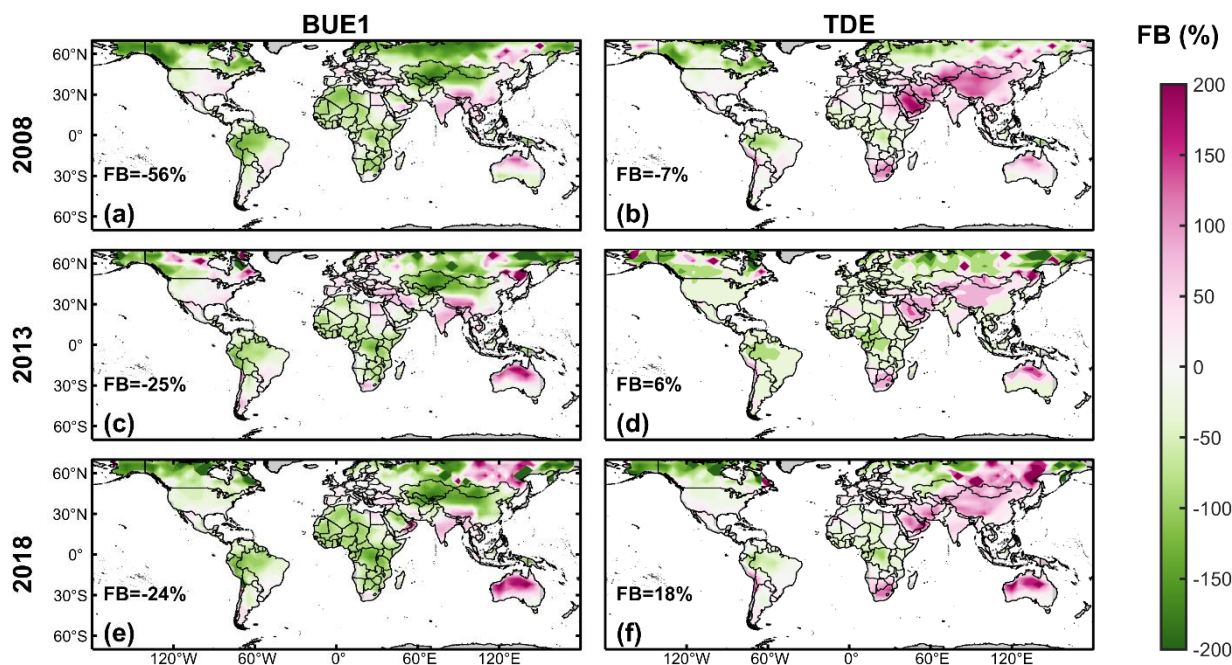


307

308 **Figure 6.** Spatial distribution of  $\text{NH}_3$  lifetime (h) diagnosed from GEOS-Chem (Eq. (2)) within the  $70^\circ\text{N}$ - $70^\circ\text{S}$  during 2008-2018.

309 **Fig. 6** shows the spatial variation in  $\text{NH}_3$  lifetime diagnosed from the GEOS-Chem simulation. Short  $\text{NH}_3$  lifetimes ( $< 10$  h)  
310 are found mainly in northern high latitudes. Short lifetime in eastern China is due to high wet  $\text{NH}_4^+$  deposition velocity,  
311 although some regional studies suggested an overestimation of deposition fluxes by the model especially in forest areas (e.g.,  
312 Yangtze River basin) (Zhao et al., 2017; Xu et al., 2018). Very long  $\text{NH}_3$  lifetime ( $> 100$  h) occurs over Sahara and Australia,  
313 where dry conditions result in slow wet deposition.

314 We then evaluate the consistency of  $\text{NH}_3$  emissions derived from varied methods with IASI observations using full GEOS-  
315 Chem simulations in the selected years of 2008, 2013, and 2018. Results are shown in **Fig. 7** (fractional bias, FB) and **Table**  
316 **S2** (number of valid grid cells,  $R^2$ , and root mean square error). The full-chemistry GEOS-Chem simulations driven the prior  
317 emissions (BUE1) tends to underestimate  $\text{NH}_3$  column density (mean FB  $\sim 30\%$ ), while that driven by our TDE emission  
318 estimates with improved  $\text{NH}_3$  lifetime calculation achieves better consistency with observations (mean FB  $\sim 10\%$ ). The fact  
319 that the TDE is more consistent with IASI observations demonstrates the superiority of the improved top-down method.



320

321 **Figure 7.** Fractional biases of simulated  $\text{NH}_3$  column densities from GEOS-Chem simulations driven by (a, c, e) BUE1 and (b, d, f) TDE  
322 for the year (a-b) 2008, (d-e) 2013 and (g-h) 2018, against IASI observations. Global average FBs (%) for each year are inset.

#### 323 4 Conclusions

324 This study quantifies global ammonia ( $\text{NH}_3$ ) fluxes monthly from 2008 to 2018 at  $4^\circ \times 5^\circ$  resolution, through a fast top-  
325 down method that incorporates IASI satellite observations and GEOS-Chem model simulations. The top-down method  
326 updates the prior  $\text{NH}_3$  emissions with a correction term positively proportional to the difference of the observed and  
327 simulated  $\text{NH}_3$  concentrations, and inversely proportional to the lifetime diagnosed from a CTM. This method revises  
328 previously proposed fast top-down methods in two aspects. First, we account for thermodynamic equilibrium within the  $\text{NH}_x$   
329 family in diagnosing  $\text{NH}_3$  lifetime, while previous studies either assume a globally constant lifetime or treat conversion from  
330  $\text{NH}_3$  to  $\text{NH}_4^+$  as a terminal sink. Second, our formulation linearizes the column-emission relationship at prior emissions as  
331 opposed to zero emissions in the previous method, which in general reduces errors from the local mass balance  
332 approximation. Another improvement is that we apply several data filtering procedures to exclude unreliable top-down  
333 results that are not sufficiently constrained by observations or affected by large deviations from the local mass balance  
334 assumption.

335 We apply this improved fast top-down method to IASI  $\text{NH}_3$  column observations from 2008 to 2018. We find that the  
336 bottom-up inventory (BUE1) underestimates  $\text{NH}_3$  emission over South America (62 %) and tropical Africa (69 %), but  
337 overestimates over India (14 %) and Canada (33 %). The bottom-up inventory agrees with the top-down estimate over the  
338 U.S., Europe, and eastern China (i.e., within 10 %). Our analysis also shows significant increases in India ( $13\% \text{ decade}^{-1}$ ),



339 tropical Africa (33 % decade<sup>-1</sup>), and South America (18 % decade<sup>-1</sup>) during the study period, consistent with intensifying  
340 agricultural activities over these regions. An analysis of agricultural statistics suggests that the increase in tropical Africa is  
341 likely driven by growing livestock population and that in South America by increasing fertilizer usage.

342 We show that large increases in NH<sub>3</sub> concentrations in eastern China is mainly driven by rapid decreases in SO<sub>2</sub> emissions in  
343 recent years. By accounting for observed SO<sub>2</sub> columns, we find that NH<sub>3</sub> emissions from eastern China is significantly  
344 decreasing during 2008-2018 (-19 % decade<sup>-1</sup>), with a larger negative trend after 2013 (-28 % decade<sup>-1</sup>), as compared to a  
345 significant positive trend (61 % decade<sup>-1</sup>) derived from assimilating only NH<sub>3</sub> data. Similarly, a lack of trend in observed  
346 NH<sub>3</sub> concentrations over India is due to concurrent increases in SO<sub>2</sub> and NH<sub>3</sub> emissions. After including observed SO<sub>2</sub>  
347 columns in the calculation, we estimate a 13 % increase in NH<sub>3</sub> emissions over India, with a significant post-2013 positive  
348 trend (30 % decade<sup>-1</sup>). These results from assimilating both NH<sub>3</sub> and SO<sub>2</sub> data is more consistent with the agricultural  
349 statistics in China and India.

350 Our estimate for global total NH<sub>3</sub> emission is 79 (71-96) Tg a<sup>-1</sup>, about 30 % higher than the BUE1 estimate. This contrasts  
351 with a much higher estimate (180 Tg a<sup>-1</sup>) derived from Evangeliou et al. (2021) also using IASI data. The discrepancy can be  
352 primarily attributed to a longer NH<sub>3</sub> lifetime (i.e., global average 21 h) diagnosed in our method, which represents a greater  
353 sensitivity of NH<sub>3</sub> column to emissions, and a more conservative data filtering strategy, which removes potentially unreliable  
354 top-down results. Our diagnosis of NH<sub>3</sub> lifetime is an improvement over Evangeliou et al. (2021), by accounting for the  
355 thermodynamic equilibrium between gas phase NH<sub>3</sub> and aerosol phase NH<sub>4</sub><sup>+</sup> in our formula. We show with full chemistry  
356 simulations, our top-down estimate achieves better consistency with IASI observations, compared to the bottom-up emission  
357 inventory (BUE1).

358

359 *Data availability.*

360 The IASI L2 ammonia satellite observations are available at the AERIS data infrastructure (<https://iasi.aeris-data.fr/>). The  
361 ERA5 skin temperature and GFAS fire emission can be request through Copernicus Climate Data Store  
362 (<https://cds.climate.copernicus.eu/cdsapp#!/home>). Agricultural data are available through Food and Agriculture  
363 Organization of the United Nations (FAO) (<http://www.fao.org/faostat>). The GEOS-Chem model can be retrieved from  
364 10.5281/zenodo.3974569. All the other data and scripts used for the present publication can be obtained from the  
365 corresponding author upon request.

366 *Author contributions.*

367 ZL and YZ designed the study. ZL performed the simulations and analyses and wrote and coordinated the paper. WC  
368 contributed to the model simulations for consistency evaluation. LC, MVD, and PFC developed the IASI-NH<sub>3</sub> satellite  
369 product. ZL and YZ wrote the paper with inputs from all authors.



370 *Acknowledgements.*

371 This study is supported by Westlake University. We thank the High-Performance Computing Center of Westlake University  
372 for the facility support and technical assistance. We acknowledge the AERIS data infrastructure <https://www.aeris-data.fr> for  
373 providing access to the IASI data. The IASI L1c data are received through the EUMETCast near real-time data distribution  
374 service. Research at ULB was supported by the Belgian State Federal Office for Scientific, Technical and Cultural Affairs  
375 (Prodex HIRS) and the Air Liquide Foundation (TAPIR project). LC is Research Associate supported by the Belgian F.R.S.-  
376 FNRS. Hersbach et al., (2020) was downloaded from the Copernicus Climate Change Service (C3S) Climate Data Store. The  
377 results contain modified Copernicus Climate Change Service information 2020. Neither the European Commission nor  
378 ECMWF is responsible for any use that may be made of the Copernicus information or data it contains. IASI is a joint  
379 mission of Eumetsat and the “Centre National d’Études Spatiales” (CNES, France). We acknowledge the constructive  
380 comments and suggestions from Prof. Peter Hess from the Cornell University and Dr. Yi Wang from the University of Iowa.  
381 We also acknowledge Dr. Nikolaos Evangeliou from Norwegian Institute for Air Research for providing his NH<sub>3</sub> emission  
382 flux data and for discussions with ZL.

383 **References**

- 384 Acharja, P., Ali, K., Ghude, S. D., Sinha, V., Sinha, B., Kulkarni, R., Gultepe, I., and Rajeevan, M. N.:  
385 Enhanced secondary aerosol formation driven by excess ammonia during fog episodes in Delhi, India,  
386 *Chemosphere*, 289, 133155, [10.1016/j.chemosphere.2021.133155](https://doi.org/10.1016/j.chemosphere.2021.133155), 2022.
- 387 Amos, H. M., Jacob, D. J., Holmes, C. D., Fisher, J. A., Wang, Q., Yantosca, R. M., Corbitt, E. S.,  
388 Galarneau, E., Rutter, A. P., Gustin, M. S., Steffen, A., Schauer, J. J., Graydon, J. A., Louis, V. L. S.,  
389 Talbot, R. W., Edgerton, E. S., Zhang, Y., and Sunderland, E. M.: Gas-particle partitioning of  
390 atmospheric Hg(II) and its effect on global mercury deposition, *Atmospheric Chemistry and Physics*, 12,  
391 591-603, [10.5194/acp-12-591-2012](https://doi.org/10.5194/acp-12-591-2012), 2012.
- 392 Behera, S. N., Sharma, M., Aneja, V. P., and Balasubramanian, R.: Ammonia in the atmosphere: a  
393 review on emission sources, atmospheric chemistry and deposition on terrestrial bodies, *Environ Sci*  
394 *Pollut Res Int*, 20, 8092-8131, [10.1007/s11356-013-2051-9](https://doi.org/10.1007/s11356-013-2051-9), 2013.
- 395 Bey, I., Jacob, D. J., Yantosca, R. M., Logan, J. A., Field, B. D., Fiore, A. M., Li, Q., Liu, H. Y.,  
396 Mickley, L. J., and Schultz, M. G.: Global modeling of tropospheric chemistry with assimilated  
397 meteorology: Model description and evaluation, *Journal of Geophysical Research: Atmospheres*, 106,  
398 23073-23095, [10.1029/2001jd000807](https://doi.org/10.1029/2001jd000807), 2001.
- 399 Bouwman, A. F., Lee, D. S., Asman, W. A. H., Dentener, F. J., Van Der Hoek, K. W., and Olivier, J. G.  
400 J.: A global high-resolution emission inventory for ammonia, *Global Biogeochemical Cycles*, 11, 561-  
401 587, [10.1029/97gb02266](https://doi.org/10.1029/97gb02266), 1997.



- 402 Cao, H., Henze, D. K., Shephard, M. W., Dammers, E., Cady-Pereira, K., Alvarado, M., Lonsdale, C.,  
403 Luo, G., Yu, F., Zhu, L., Danielson, C. G., and Edgerton, E. S.: Inverse modeling of NH<sub>3</sub> sources using  
404 CrIS remote sensing measurements, *Environmental Research Letters*, 15, 10.1088/1748-9326/abb5cc,  
405 2020.
- 406 Chen, Y., Morton, D. C., Jin, Y., Collatz, G. J., Kasibhatla, P. S., van der Werf, G. R., DeFries, R. S.,  
407 and Randerson, J. T.: Long-term trends and interannual variability of forest, savanna and agricultural  
408 fires in South America, *Carbon Management*, 4, 617-638, 10.4155/cmt.13.61, 2014.
- 409 Chen, Y., Zhang, L., Henze, D. K., Zhao, Y., Lu, X., Winiwarter, W., Guo, Y., Liu, X., Wen, Z., Pan,  
410 Y., and Song, Y.: Interannual variation of reactive nitrogen emissions and their impacts on PM<sub>2.5</sub> air  
411 pollution in China during 2005–2015, *Environmental Research Letters*, 16, 10.1088/1748-9326/ac3695,  
412 2021a.
- 413 Chen, Y., Shen, H., Kaiser, J., Hu, Y., Capps, S. L., Zhao, S., Hakami, A., Shih, J.-S., Pavur, G. K.,  
414 Turner, M. D., Henze, D. K., Resler, J., Nenes, A., Napelenok, S. L., Bash, J. O., Fahey, K. M.,  
415 Carmichael, G. R., Chai, T., Clarisse, L., Coheur, P.-F., Van Damme, M., and Russell, A. G.: High-  
416 resolution hybrid inversion of IASI ammonia columns to constrain US ammonia emissions using the  
417 CMAQ adjoint model, *Atmospheric Chemistry and Physics*, 21, 2067-2082, 10.5194/acp-21-2067-2021,  
418 2021b.
- 419 Clerbaux, C., Boynard, A., Clarisse, L., George, M., Hadji-Lazaro, J., Herbin, H., Hurtmans, D.,  
420 Pommier, M., Razavi, A., Turquety, S. J. A. C., and Physics: Monitoring of atmospheric composition  
421 using the thermal infrared IASI/MetOp sounder, *Atmospheric Chemistry and Physics*, 9, 6041-6054,  
422 2009.
- 423 Crippa, M., Solazzo, E., Huang, G., Guizzardi, D., Koffi, E., Muntean, M., Schieberle, C., Friedrich, R.,  
424 and Janssens-Maenhout, G.: High resolution temporal profiles in the Emissions Database for Global  
425 Atmospheric Research, *Sci Data*, 7, 121, 10.1038/s41597-020-0462-2, 2020.
- 426 Dirnbock, T., Grandin, U., Bernhardt-Romermann, M., Beudert, B., Canullo, R., Forsius, M., Grabner,  
427 M. T., Holmberg, M., Kleemola, S., Lundin, L., Mirtl, M., Neumann, M., Pompei, E., Salemaa, M.,  
428 Starlinger, F., Staszewski, T., and Uzieblo, A. K.: Forest floor vegetation response to nitrogen  
429 deposition in Europe, *Glob Chang Biol*, 20, 429-440, 10.1111/gcb.12440, 2014.
- 430 Erisman, J. W. J. S.: How ammonia feeds and pollutes the world, *Science*, 374, 685-686, 2021.
- 431 Evangeliou, N., Balkanski, Y., Eckhardt, S., Cozic, A., Van Damme, M., Coheur, P.-F., Clarisse, L.,  
432 Shephard, M. W., Cady-Pereira, K. E., and Hauglustaine, D.: 10-year satellite-constrained fluxes of  
433 ammonia improve performance of chemistry transport models, *Atmospheric Chemistry and Physics*, 21,  
434 4431-4451, 10.5194/acp-21-4431-2021, 2021.
- 435 Fountoukis, C., Nenes, A. J. A. C., and Physics: ISORROPIA II: a computationally efficient  
436 thermodynamic equilibrium model for K<sup>+</sup>–Ca<sup>2+</sup>–Mg<sup>2+</sup>–NH<sub>4</sub><sup>+</sup>–Na<sup>+</sup>–SO<sub>4</sub><sup>2-</sup>–NO<sub>3</sub><sup>-</sup>–Cl<sup>-</sup>–H<sub>2</sub>O  
437 aerosols, *Atmospheric Chemistry and Physics*, 7, 4639-4659, 2007.



- 438 Franco, B., Clarisse, L., Stavrou, T., Müller, J. F., Van Damme, M., Whitburn, S., Hadji - Lazaro, J.,  
439 Hurtmans, D., Taraborrelli, D., Clerbaux, C., and Coheur, P. F.: A General Framework for Global  
440 Retrievals of Trace Gases From IASI: Application to Methanol, Formic Acid, and PAN, *Journal of*  
441 *Geophysical Research: Atmospheres*, 123, 10.1029/2018jd029633, 2018.
- 442 Fu, X., Wang, S., Xing, J., Zhang, X., Wang, T., and Hao, J.: Increasing Ammonia Concentrations  
443 Reduce the Effectiveness of Particle Pollution Control Achieved via SO<sub>2</sub> and NO<sub>x</sub> Emissions  
444 Reduction in East China, *Environmental Science & Technology Letters*, 4, 221-227,  
445 10.1021/acs.estlett.7b00143, 2017.
- 446 Gelaro, R., McCarty, W., Suarez, M. J., Todling, R., Molod, A., Takacs, L., Randles, C., Darmenov, A.,  
447 Bosilovich, M. G., Reichle, R., Wargan, K., Coy, L., Cullather, R., Draper, C., Akella, S., Buchard, V.,  
448 Conaty, A., da Silva, A., Gu, W., Kim, G. K., Koster, R., Lucchesi, R., Merkova, D., Nielsen, J. E.,  
449 Partyka, G., Pawson, S., Putman, W., Rienecker, M., Schubert, S. D., Sienkiewicz, M., and Zhao, B.:  
450 The Modern-Era Retrospective Analysis for Research and Applications, Version 2 (MERRA-2), *J Clim*,  
451 Volume 30, 5419-5454, 10.1175/JCLI-D-16-0758.1, 2017.
- 452 Gu, B., Zhang, L., Van Dingenen, R., Vieno, M., Van Grinsven, H. J., Zhang, X., Zhang, S., Chen, Y.,  
453 Wang, S., and Ren, C. J. S.: Abating ammonia is more cost-effective than nitrogen oxides for mitigating  
454 PM<sub>2.5</sub> air pollution, *Science*, 374, 758-762, 2021.
- 455 Guenther, A. B., Jiang, X., Heald, C. L., Sakulyanontvittaya, T., Duhl, T., Emmons, L. K., and Wang,  
456 X.: The Model of Emissions of Gases and Aerosols from Nature version 2.1 (MEGAN2.1): an extended  
457 and updated framework for modeling biogenic emissions, *Geoscientific Model Development*, 5, 1471-  
458 1492, 10.5194/gmd-5-1471-2012, 2012.
- 459 Guo, X., Wang, R., Pan, D., Zondlo, M. A., Clarisse, L., Van Damme, M., Whitburn, S., Coheur, P. F.,  
460 Clerbaux, C., Franco, B., Golston, L. M., Wendt, L., Sun, K., Tao, L., Miller, D., Mikoviny, T., Müller,  
461 M., Wisthaler, A., Tevlin, A. G., Murphy, J. G., Nowak, J. B., Roscioli, J. R., Volkamer, R., Kille, N.,  
462 Neuman, J. A., Eilerman, S. J., Crawford, J. H., Yacovitch, T. I., Barrick, J. D., and Scarino, A. J.:  
463 Validation of IASI Satellite Ammonia Observations at the Pixel Scale Using In Situ Vertical Profiles,  
464 *Journal of Geophysical Research: Atmospheres*, 126, 10.1029/2020jd033475, 2021.
- 465 Hersbach, H., Bell, B., Berrisford, P., Hirahara, S., Horányi, A., Muñoz - Sabater, J., Nicolas, J.,  
466 Peubey, C., Radu, R., Schepers, D., Simmons, A., Soci, C., Abdalla, S., Abellan, X., Balsamo, G.,  
467 Bechtold, P., Biavati, G., Bidlot, J., Bonavita, M., Chiara, G., Dahlgren, P., Dee, D., Diamantakis, M.,  
468 Dragani, R., Flemming, J., Forbes, R., Fuentes, M., Geer, A., Haimberger, L., Healy, S., Hogan, R. J.,  
469 Hólm, E., Janisková, M., Keeley, S., Laloyaux, P., Lopez, P., Lupu, C., Radnoti, G., Rosnay, P., Rozum,  
470 I., Vamborg, F., Villaume, S., and Thépaut, J. N.: The ERA5 global reanalysis, *Quarterly Journal of the*  
471 *Royal Meteorological Society*, 146, 1999-2049, 10.1002/qj.3803, 2020.
- 472 Hickman, J. E., Andela, N., Tsigaridis, K., Galy-Lacaux, C., Ossouhou, M., and Bauer, S. E.: Reductions  
473 in NO<sub>2</sub> burden over north equatorial Africa from decline in biomass burning in spite of growing fossil  
474 fuel use, 2005 to 2017, *Proc Natl Acad Sci U S A*, 118, 10.1073/pnas.2002579118, 2021a.



- 475 Hickman, J. E., Andela, N., Dammers, E., Clarisse, L., Coheur, P.-F., Van Damme, M., Di Vittorio, C.  
476 A., Ossohou, M., Galy-Lacaux, C., Tsigaridis, K., and Bauer, S. E.: Changes in biomass burning,  
477 wetland extent, or agriculture drive atmospheric  $\text{NH}_3$  trends in select African  
478 regions, *Atmospheric Chemistry and Physics*, 21, 16277-16291, 10.5194/acp-21-16277-2021, 2021b.
- 479 Hoesly, R. M., Smith, S. J., Feng, L., Klimont, Z., Janssens-Maenhout, G., Pitkanen, T., Seibert, J. J.,  
480 Vu, L., Andres, R. J., Bolt, R. M., Bond, T. C., Dawidowski, L., Kholod, N., Kurokawa, J.-i., Li, M.,  
481 Liu, L., Lu, Z., Moura, M. C. P., O'Rourke, P. R., and Zhang, Q.: Historical (1750–2014) anthropogenic  
482 emissions of reactive gases and aerosols from the Community Emissions Data System (CEDS),  
483 *Geoscientific Model Development*, 11, 369-408, 10.5194/gmd-11-369-2018, 2018.
- 484 Höpfner, M., Ungermann, J., Borrmann, S., Wagner, R., Spang, R., Riese, M., Stiller, G., Appel, O.,  
485 Batenburg, A. M., Bucci, S., Cairo, F., Dragoneas, A., Friedl-Vallon, F., Hünig, A., Johansson, S.,  
486 Krasauskas, L., Legras, B., Leisner, T., Mahnke, C., Möhler, O., Molleker, S., Müller, R., Neubert, T.,  
487 Orphal, J., Preusse, P., Rex, M., Saathoff, H., Strohm, F., Weigel, R., and Wohltmann, I.: Ammonium  
488 nitrate particles formed in upper troposphere from ground ammonia sources during Asian monsoons,  
489 *Nature Geoscience*, 12, 608-612, 10.1038/s41561-019-0385-8, 2019.
- 490 Keywood, M., Kanakidou, M., Stohl, A., Dentener, F., Grassi, G., Meyer, C. P., Torseth, K., Edwards,  
491 D., Thompson, A. M., Lohmann, U., and Burrows, J.: Fire in the Air: Biomass Burning Impacts in a  
492 Changing Climate, *Critical Reviews in Environmental Science and Technology*, 43, 40-83,  
493 10.1080/10643389.2011.604248, 2011.
- 494 Lachatre, M., Fortems-Cheiney, A., Foret, G., Siour, G., Dufour, G., Clarisse, L., Clerbaux, C., Coheur,  
495 P.-F., Van Damme, M., and Beekmann, M.: The unintended consequence of  
496  $\text{SO}_2$  and  $\text{NO}_2$  regulations over China: increase of  
497 ammonia levels and impact on  $\text{PM}_{2.5}$  concentrations, *Atmospheric Chemistry*  
498 *and Physics*, 19, 6701-6716, 10.5194/acp-19-6701-2019, 2019.
- 499 Li, M., Zhang, Q., Kurokawa, J.-i., Woo, J.-H., He, K., Lu, Z., Ohara, T., Song, Y., Streets, D. G.,  
500 Carmichael, G. R., Cheng, Y., Hong, C., Huo, H., Jiang, X., Kang, S., Liu, F., Su, H., and Zheng, B.:  
501 MIX: a mosaic Asian anthropogenic emission inventory under the international collaboration  
502 framework of the MICS-Asia and HTAP, *Atmospheric Chemistry and Physics*, 17, 935-963,  
503 10.5194/acp-17-935-2017, 2017.
- 504 Liu, M., Huang, X., Song, Y., Xu, T., Wang, S., Wu, Z., Hu, M., Zhang, L., Zhang, Q., Pan, Y., Liu, X.,  
505 and Zhu, T.: Rapid  $\text{SO}_2$  emission reductions significantly increase tropospheric  
506 ammonia concentrations over the North China Plain, *Atmospheric Chemistry and Physics*, 18, 17933-  
507 17943, 10.5194/acp-18-17933-2018, 2018.
- 508 Liu, X., Zhang, Y., Han, W., Tang, A., Shen, J., Cui, Z., Vitousek, P., Erisman, J. W., Goulding, K.,  
509 Christie, P., Fangmeier, A., and Zhang, F.: Enhanced nitrogen deposition over China, *Nature*, 494, 459-  
510 462, 10.1038/nature11917, 2013.



- 511 Ma, R., Zou, J., Han, Z., Yu, K., Wu, S., Li, Z., Liu, S., Niu, S., Horwath, W. R., and Zhu-Barker, X.:  
512 Global soil-derived ammonia emissions from agricultural nitrogen fertilizer application: A refinement  
513 based on regional and crop-specific emission factors, *Glob Chang Biol*, 27, 855-867,  
514 10.1111/gcb.15437, 2021.
- 515 Ma, X., Yu, F., and Luo, G.: Aerosol direct radiative forcing based on GEOS-Chem-APM and  
516 uncertainties, *Atmospheric Chemistry and Physics*, 12, 5563-5581, 10.5194/acp-12-5563-2012, 2012.
- 517 Marais, E. A. and Wiedinmyer, C.: Air Quality Impact of Diffuse and Inefficient Combustion Emissions  
518 in Africa (DICE-Africa), *Environ Sci Technol*, 50, 10739-10745, 10.1021/acs.est.6b02602, 2016.
- 519 Marais, E. A., Pandey, A. K., Van Damme, M., Clarisse, L., Coheur, P. F., Shephard, M. W., Cady -  
520 Pereira, K. E., Misselbrook, T., Zhu, L., Luo, G., and Yu, F.: UK Ammonia Emissions Estimated With  
521 Satellite Observations and GEOS - Chem, *Journal of Geophysical Research: Atmospheres*, 126,  
522 10.1029/2021jd035237, 2021.
- 523 Park, R. J.: Natural and transboundary pollution influences on sulfate-nitrate-ammonium aerosols in the  
524 United States: Implications for policy, *Journal of Geophysical Research*, 109, 10.1029/2003jd004473,  
525 2004.
- 526 Paulot, F., Jacob, D. J., Pinder, R. W., Bash, J. O., Travis, K., and Henze, D. K.: Ammonia emissions in  
527 the United States, European Union, and China derived by high-resolution inversion of ammonium wet  
528 deposition data: Interpretation with a new agricultural emissions inventory (MASAGE\_NH3), *Journal*  
529 *of Geophysical Research: Atmospheres*, 119, 4343-4364, 10.1002/2013jd021130, 2014.
- 530 Pavlovic, R., Chen, J., Anderson, K., Moran, M. D., Beaulieu, P. A., Davignon, D., and Cousineau, S.:  
531 The FireWork air quality forecast system with near-real-time biomass burning emissions: Recent  
532 developments and evaluation of performance for the 2015 North American wildfire season, *J Air Waste*  
533 *Manag Assoc*, 66, 819-841, 10.1080/10962247.2016.1158214, 2016.
- 534 Qu, Z., Henze, D. K., Li, C., Theys, N., Wang, Y., Wang, J., Wang, W., Han, J., Shim, C., Dickerson, R.  
535 R., and Ren, X.: SO<sub>2</sub> Emission Estimates Using OMI SO<sub>2</sub> Retrievals for 2005-2017, *J Geophys Res*  
536 *Atmos*, 124, 8336-8359, 10.1029/2019JD030243, 2019.
- 537 Riddick, S., Ward, D., Hess, P., Mahowald, N., Massad, R., and Holland, E.: Estimate of changes in  
538 agricultural terrestrial nitrogen pathways and ammonia emissions from 1850 to present in the  
539 Community Earth System Model, *Biogeosciences*, 13, 3397-3426, 10.5194/bg-13-3397-2016, 2016.
- 540 Schiferl, L. D., Heald, C. L., Van Damme, M., Clarisse, L., Clerbaux, C., Coheur, P.-F., Nowak, J. B.,  
541 Neuman, J. A., Herndon, S. C., Roscioli, J. R., and Eilerman, S. J.: Interannual variability of ammonia  
542 concentrations over the United States:  
543 sources and implications, *Atmospheric Chemistry and Physics*, 16, 12305-12328, 10.5194/acp-16-  
544 12305-2016, 2016.



- 545 Stevens, C. J., Dupre, C., Dorland, E., Gaudnik, C., Gowing, D. J., Bleeker, A., Diekmann, M., Alard,  
546 D., Bobbink, R., Fowler, D., Corcket, E., Mountford, J. O., Vandvik, V., Aarrestad, P. A., Muller, S.,  
547 and Dise, N. B.: Nitrogen deposition threatens species richness of grasslands across Europe, *Environ*  
548 *Pollut*, 158, 2940-2945, 10.1016/j.envpol.2010.06.006, 2010.
- 549 Sun, W., Shao, M., Granier, C., Liu, Y., Ye, C. S., and Zheng, J. Y.: Long-Term Trends of  
550 Anthropogenic SO<sub>2</sub>
- 551 , NO<sub>x</sub>
- 552 , CO, and NMVOCs Emissions in China, *Earth's Future*, 6, 1112-1133, 10.1029/2018ef000822, 2018.
- 553 Sutton, M. A., Reis, S., Riddick, S. N., Dragosits, U., Nemitz, E., Theobald, M. R., Tang, Y. S., Braban,  
554 C. F., Viero, M., Dore, A. J., Mitchell, R. F., Wanless, S., Daunt, F., Fowler, D., Blackall, T. D.,  
555 Milford, C., Flechard, C. R., Loubet, B., Massad, R., Cellier, P., Personne, E., Coheur, P. F., Clarisse, L.,  
556 Van Damme, M., Ngadi, Y., Clerbaux, C., Skjoth, C. A., Geels, C., Hertel, O., Wichink Kruit, R. J.,  
557 Pinder, R. W., Bash, J. O., Walker, J. T., Simpson, D., Horvath, L., Misselbrook, T. H., Bleeker, A.,  
558 Dentener, F., and de Vries, W.: Towards a climate-dependent paradigm of ammonia emission and  
559 deposition, *Philos Trans R Soc Lond B Biol Sci*, 368, 20130166, 10.1098/rstb.2013.0166, 2013.
- 560 Van Damme, M., Whitburn, S., Clarisse, L., Clerbaux, C., Hurtmans, D., and Coheur, P.-F.: Version 2  
561 of the IASI NH<sub>3</sub>; neural network retrieval algorithm: near-real-time and  
562 reanalysed datasets, *Atmospheric Measurement Techniques*, 10, 4905-4914, 10.5194/amt-10-4905-2017,  
563 2017.
- 564 Van Damme, M., Clarisse, L., Whitburn, S., Hadji-Lazaro, J., Hurtmans, D., Clerbaux, C., and Coheur,  
565 P. F.: Industrial and agricultural ammonia point sources exposed, *Nature*, 564, 99-103, 10.1038/s41586-  
566 018-0747-1, 2018.
- 567 Van Damme, M., Clarisse, L., Heald, C. L., Hurtmans, D., Ngadi, Y., Clerbaux, C., Dolman, A. J.,  
568 Erisman, J. W., and Coheur, P. F.: Global distributions, time series and error characterization of  
569 atmospheric ammonia (NH<sub>3</sub>) from IASI satellite observations, *Atmospheric*  
570 *Chemistry and Physics*, 14, 2905-2922, 10.5194/acp-14-2905-2014, 2014.
- 571 Van Damme, M., Clarisse, L., Franco, B., Sutton, M. A., Erisman, J. W., Wichink Kruit, R., van Zanten,  
572 M., Whitburn, S., Hadji-Lazaro, J., Hurtmans, D., Clerbaux, C., and Coheur, P.-F.: Global, regional and  
573 national trends of atmospheric ammonia derived from a decadal (2008–2018) satellite record,  
574 *Environmental Research Letters*, 16, 10.1088/1748-9326/abd5e0, 2021.
- 575 Van Damme, M., Clarisse, L., Dammers, E., Liu, X., Nowak, J. B., Clerbaux, C., Flechard, C. R., Galy-  
576 Lacaux, C., Xu, W., Neuman, J. A., Tang, Y. S., Sutton, M. A., Erisman, J. W., and Coheur, P. F.:  
577 Towards validation of ammonia (NH<sub>3</sub>) measurements from the IASI satellite,  
578 *Atmospheric Measurement Techniques*, 8, 1575-1591, 10.5194/amt-8-1575-2015, 2015.



- 579 van der Graaf, S., Dammers, E., Segers, A., Kranenburg, R., Schaap, M., Shephard, M. W., and Erisman,  
580 J. W.: Data assimilation of CrIS NH<sub>3</sub> satellite observations for improving  
581 spatiotemporal NH<sub>3</sub> distributions in LOTOS-EUROS, *Atmospheric Chemistry  
582 and Physics*, 22, 951-972, 10.5194/acp-22-951-2022, 2022.
- 583 van der Werf, G. R., Randerson, J. T., Giglio, L., van Leeuwen, T. T., Chen, Y., Rogers, B. M., Mu, M.,  
584 van Marle, M. J. E., Morton, D. C., Collatz, G. J., Yokelson, R. J., and Kasibhatla, P. S.: Global fire  
585 emissions estimates during 1997–2016, *Earth System Science Data*, 9, 697-720, 10.5194/essd-9-697-  
586 2017, 2017.
- 587 Vira, J., Hess, P., Ossohou, M., and Galy-Lacaux, C., 10.5194/acp-2021-538,
- 588 Wang, Q., Jacob, D. J., Fisher, J. A., Mao, J., Leibensperger, E. M., Carouge, C. C., Le Sager, P.,  
589 Kondo, Y., Jimenez, J. L., Cubison, M. J., and Doherty, S. J.: Sources of carbonaceous aerosols and  
590 deposited black carbon in the Arctic in winter-spring: implications for radiative forcing, *Atmospheric  
591 Chemistry and Physics*, 11, 12453-12473, 10.5194/acp-11-12453-2011, 2011.
- 592 Wang, Y. and Wang, J.: Tropospheric SO<sub>2</sub> and NO<sub>2</sub> in 2012–2018: Contrasting views of two sensors  
593 (OMI and OMPS) from space, *Atmospheric Environment*, 223, 10.1016/j.atmosenv.2019.117214, 2020.
- 594 Warner, J. X., Dickerson, R. R., Wei, Z., Strow, L. L., Wang, Y., and Liang, Q.: Increased atmospheric  
595 ammonia over the world's major agricultural areas detected from space, *Geophys Res Lett*, 44, 2875-  
596 2884, 10.1002/2016GL072305, 2017.
- 597 Wesely, M.: Parameterization of surface resistances to gaseous dry deposition in regional-scale  
598 numerical models☆, *Atmospheric Environment*, 41, 52-63, 10.1016/j.atmosenv.2007.10.058, 2007.
- 599 Whitburn, S., Van Damme, M., Clarisse, L., Bauduin, S., Heald, C. L., Hadji-Lazaro, J., Hurtmans, D.,  
600 Zondlo, M. A., Clerbaux, C., and Coheur, P. F.: A flexible and robust neural network IASI-  
601 NH<sub>3</sub> retrieval algorithm, *Journal of Geophysical Research: Atmospheres*, 121, 6581-6599,  
602 10.1002/2016jd024828, 2016.
- 603 Xu, W., Zhao, Y., Liu, X., Dore, A. J., Zhang, L., Liu, L., and Cheng, M.: Atmospheric nitrogen  
604 deposition in the Yangtze River basin: Spatial pattern and source attribution, *Environ Pollut*, 232, 546-  
605 555, 10.1016/j.envpol.2017.09.086, 2018.
- 606 Zhai, S., Jacob, D. J., Wang, X., Liu, Z., Wen, T., Shah, V., Li, K., Moch, J. M., Bates, K. H., Song, S.,  
607 Shen, L., Zhang, Y., Luo, G., Yu, F., Sun, Y., Wang, L., Qi, M., Tao, J., Gui, K., Xu, H., Zhang, Q.,  
608 Zhao, T., Wang, Y., Lee, H. C., Choi, H., and Liao, H.: Control of particulate nitrate air pollution in  
609 China, *Nature Geoscience*, 14, 389-395, 10.1038/s41561-021-00726-z, 2021.
- 610 Zhang, L., Chen, Y., Zhao, Y., Henze, D. K., Zhu, L., Song, Y., Paulot, F., Liu, X., Pan, Y., Lin, Y., and  
611 Huang, B.: Agricultural ammonia emissions in China: reconciling bottom-up and top-down estimates,  
612 *Atmospheric Chemistry and Physics*, 18, 339-355, 10.5194/acp-18-339-2018, 2018.



- 613 Zhang, X., Wu, Y., Liu, X., Reis, S., Jin, J., Dragosits, U., Van Damme, M., Clarisse, L., Whitburn, S.,  
614 Coheur, P. F., and Gu, B.: Ammonia Emissions May Be Substantially Underestimated in China,  
615 Environ Sci Technol, 51, 12089-12096, 10.1021/acs.est.7b02171, 2017.
- 616 Zhao, Y., Duan, L., Xing, J., Larssen, T., Nielsen, C. P., and Hao, J.: Soil acidification in China: is  
617 controlling SO<sub>2</sub> emissions enough?, 2009.
- 618 Zhao, Y., Zhang, L., Chen, Y., Liu, X., Xu, W., Pan, Y., and Duan, L.: Atmospheric nitrogen deposition  
619 to China: A model analysis on nitrogen budget and critical load exceedance, Atmospheric Environment,  
620 153, 32-40, 10.1016/j.atmosenv.2017.01.018, 2017.
- 621